On the effects of increased vertical mixing on the Arctic Ocean and sea ice

Xi Liang[a*], Martin Losch[b]

[a]*Key Laboratory of Research on Marine Hazards Forecasting, National Marine Environmental Forecasting Center, Beijing, China*
[b]*Alfred Wegener Institute, Helmholtz Centre for Polar and Marine Research, Bremerhaven, Germany*

Corresponding author: Xi Liang, Key Laboratory of Research on Marine Hazards Forecasting, National Marine Environmental Forecasting Center, 8 Dahuisi Road, Beijing 100081, China. (liangx@nmefc.cn)

Key Points:

- Increased vertical mixing leads to a cooling of the cold halocline layer and Atlantic Water layer.
- The reduced Arctic ocean stratification induces an adjustment of the circulation pattern.
- More vertical mixing reduces sea ice thickness all year round and decreases summertime sea ice concentration.

Abstract

Against the backdrop of Arctic sea ice decline, vertical mixing in the interior Arctic Ocean will most likely change, but it is still unclear how the Arctic Ocean and sea ice will respond. In this paper, a sea ice-ocean model with a simple parameterization for interior background mixing is used to investigate the Arctic Ocean and sea ice response to a scenario of increased vertical mixing. It is found that more vertical mixing reduces sea ice thickness all year round and decreases summertime sea ice concentration. More vertical mixing leads to a cooling of the cold halocline layer and Atlantic Water layer below. The increased vertical mixing speeds up vertical heat and salinity exchange, brings the underlying warm and saline water into the surface layer, and contributes to the sea ice decline. Vertical salinity gradient of the cold halocline layer reduces together with a much fresher Atlantic Water layer, and more volume of saline water enters the deep ocean below the Atlantic Water layer. As a result, the reduced Arctic ocean stratification leads to an adjustment of the circulation pattern. Cyclonic circulation anomalies occur in the surface layer shallower than 20 m depth and in the interior ocean deeper than 700 m depth, while anti-cyclonic circulation anomalies occur between these depths. Our study suggests that the extra heat and salinity exchange induced by more vertical mixing will have a noticeable impact on the upper ocean structure, ocean circulation and sea ice in a changing Arctic Ocean.

Key words: Arctic, vertical mixing, sea ice, ocean circulation

1. Introduction

Vertical mixing in the ocean affects the exchange of ocean heat and salinity, controls the ocean stratification, and indirectly modifies the pattern of ocean currents (Goosse et al., 1999). In the mid-latitude ocean interior away from boundaries, the observed value of vertical mixing is O (10^{-5} m^2s^{-1}) (Gregg, 1987; Kunze et al., 2006). Enhanced vertical mixing of O ($10^{-4} \sim 10^{-3}$ m^2s^{-1}) has been found over rough topography, such as ridges (Althaus et al., 2003; Klymak et al., 2006), seamounts (Kunze and Toole, 1997; Lueck and Mudge, 1997) and canyons (St. Laurent et al., 2001; Carter and Gregg, 2002). The energy for vertical mixing against stable stratification in the ocean interior is provided by the breaking of internal waves, which in turn are generated by kinetic energy input from wind and tides over rough topography (Ferrari and Wunsch, 2009).

In the Arctic Ocean, sea ice greatly reduces the effects of wind forcing. Most of the basin is north of the critical latitude of the M2 tide, thus internal wave energies generated by the interaction of barotropic tides with bathymetry are low compared to typical low-latitude levels (Simmons et al., 2004; St. Laurent et al., 2002) and hence cannot contribute much to vertical mixing. Brine rejection during the formation of sea ice is an additional Arctic-specific mechanism responsible for vertical mixing in the weakly stratified cold Arctic and sub-Arctic basins, such as the Labrador Sea and Greenland Sea. In the interior Arctic, however, brine rejection is less effective in inducing vertical mixing because of the strong stabilizing vertical salinity gradient (Yang et al., 2004). As a result, vertical mixing in the interior Arctic is relatively low. For example, mixing coefficients of O ($10^{-6} \sim 10^{-5}$ m^2s^{-1}) were estimated from microstructure measurements at the Barneo ice camp in April 2007 (Fer, 2009).

The Arctic Ocean is a quiescent ocean with the warm salty Atlantic Water layer underlying the cold halocline layer. As an important source of heat and salt in the Arctic Ocean, the Atlantic Water subducts under the cold halocline layer after entering the Arctic Ocean from Fram Strait and the Barents Sea (Steele and Boyd, 1998), then follows cyclonically the rim of the Arctic shelf with several cross-ridge intrusions (Rudels et al., 1994; Woodgate et al., 2001; Lenn et al., 2009). The Atlantic Water spreads over the whole Arctic Ocean at the depths from 200 m to 900 m (Zhang and Steele, 2007). The heat from the warm Atlantic Water inflow through Fram Strait alone would be able to melt the Arctic sea ice within four years (Turner, 2010), but the strong stratification of the cold halocline layer is thought to be a barrier that insulates the heat in the Atlantic Water layer from the mixed surface layer and sea ice. Convective mixing cannot reach the Atlantic Water layer and as a consequence, the Atlantic Water layer heat hardly contributes to the surface heat budget. The turbulent heat flux across the cold halocline layer is not significantly different from zero (Fer, 2009) and the net average heat loss from the Atlantic Water layer in the interior Arctic was estimated to be as low as 4 Wm^{-2} (Fer et al., 2010).

Sea ice melting and freezing, maintaining the cold halocline layer and the Atlantic Water layer circulation are closely linked with the Arctic Ocean stratification, as well as freshwater supply (Jensen et al., 2016). Typically, ocean stratification is eroded by vertical mixing. The role of vertical mixing in maintaining Arctic Ocean state was explored in previous studies (e.g. Zhang and Steele, 2007). In a numerical study with different vertical mixing magnitudes, the Atlantic Water layer circulation and vertical distribution of ocean properties in the cold halocline layer displayed distinct patterns. In the Canadian Basin, stronger vertical mixing weakens the ocean stratification, which will lead to an anticyclonic circulation at all depths. Weaker vertical mixing strengthens the ocean stratification, which will lead to a strong anticyclonic circulation in the upper layer and a cyclonic circulation in the lower layer (Zhang and Steele, 2007). However, the effects of varying vertical mixing on sea ice are still unclear.

The Arctic summer sea ice extent has been declining over the past several decades (Parkinson and Cavalieri, 2008; Stroeve et al., 2008; Gao et al., 2015). On one hand, the increasing open water area in the Arctic Ocean allows more wind kinetic energy input into the Arctic Ocean. Over flat bathymetry in mid-latitudes, the wind-driven mixing can reach 600 m depth and propagates even deeper with the help of anti-cyclonic eddies (Jing et al., 2011). Wind-driven mixing will likely increase according to observational evidence and could have profound effects on the Arctic circulation and sea ice (Comiso et al., 2008; Perovich, 2011). On the other hand, sea ice decline favors local surface evaporation, induces increased Arctic precipitation (Bintanja and Selten, 2014), the extra freshwater and heat storage in the surface layer due to sea ice decline supports a more stratified Arctic Ocean, which will limit vertical mixing (Davis et al., 2016). In the light of these processes with opposite effects, it is difficult to predict and to quantify the change in vertical stratification and hence interior vertical mixing.

In this paper, we assume that vertical mixing in the Arctic Ocean will increase in the future and study the isolated effects of increased vertical mixing on the Arctic ocean state and the sea ice melting-freezing cycle, especially on the upward heat transport of the Atlantic Water layer, the Atlantic Water layer circulation, and annual cycle of sea ice. The paper focuses on the ocean and sea ice responses in an Arctic sea ice-ocean model to increased vertical mixing by amplifying the vertical background diffusivity coefficient. The rest of the paper is organized as follows: section 2 describes the Arctic model and the numerical experiments. Section 3 briefly compares baseline experiment results with observations. The sea ice response to increased vertical mixing are presented in section 4 and the ocean response in section 5. Section 6 will compare the tracer tendency terms due to vertical background diffusivity with vertical advection terms. Summary and conclusion are given in section 7.

2. Model and Numerical Experiments

2.1 Coupled Sea Ice-Ocean Model

The model used in this study is an Arctic configuration of the Massachusetts Institute of Technology general circulation model (MITgcm, Marshall et al., 1997) including a sea ice module with state of the art dynamics (Losch et al., 2010). The configuration is based on that of Nguyen et al. (2011). The model domain covers the whole Arctic Ocean, it has open boundaries close to 55°N in both the Atlantic and Pacific sectors. The ocean model and sea ice module have the same horizontal grids with 420×384 grid points. The grid is locally orthogonal and has an average horizontal resolution of 18 km. The model includes 50 vertical layers, with 28 vertical levels in the top 1000 m. The thickness of the top layer is 10 m. The K-profile parameterization (KPP, Large et al., 1994) is used as the vertical mixing scheme. The ocean and sea ice parameters of our model configuration are directly taken from Nguyen et al. (2011).

The topographical data are from the U.S. National Geophysical Data Center (NGDC) 2 min global relief data set (ETOPO2, Smith and Sandwell, 1997). The initial ocean field is a climatological field derived from the World Ocean Atlas 2005 (WOA05; Locarnini et al., 2006; Antonov et al., 2006). Monthly boundary conditions of potential temperature, salinity, current, and sea-surface elevation are derived from a global configuration of the MITgcm (Menemenlis et al., 2008). Monthly mean river runoff is based on the Arctic Runoff Data Base (ARDB, Nguyen et al., 2011). We replaced the Japanese 25-year Reanalysis (JRA25; Onogi et al., 2007) in Nguyen et al. (2011), by 3-hourly atmospheric forcing data from 1979 to 2013 derived from the Japanese 55-year Reanalysis (JRA55, Kobayashi et al., 2015; Harada et al., 2016), provided by the Japan Meteorological Agency (JMA).

2.2 Numerical Experiments

The KPP vertical mixing scheme is a widely used first-order closure scheme to represent mixed layer depths and vertical mixing in open ocean regions (Large et al., 1994). The KPP scheme separates the water column into two parts, the quiescent ocean interior layer and the surface planetary boundary layer, where mixing is enhanced by surface forcing and turbulent processes. A formulation based on boundary layer similarity theory is applied to determine the depth of the actively mixing surface boundary layer. The mixing in the ocean interior is determined by local shear and static instability, internal wave breaking, and double diffusive processes. A constant background diffusivity coefficient is used to parameterize internal wave breaking.

In our model configuration, the mixing below the surface boundary layer is mostly determined by the constant background diffusivity coefficient, because vertical stability is high. With this in mind, six experiments are designed. In a reference or baseline experiment KPP001 the background diffusivity coefficient is set to 5.44×10^{-7} m^2s^{-1} following Nguyen et al. (2011). The KPP001 experiment is integrated from 1979 to 2013 with 3-hourly atmospheric forcing. The simulation fields on 1 January 1999 are used as the initial fields for five additional experiments where the vertical mixing is increased by factors of 50, 100, 150, 200, and 250 over the reference value of 5.44×10^{-7} m^2s^{-1}. These additional experiments are integrated from 1999 to 2013. In each run, daily snapshots of sea ice concentration and sea ice thickness are saved. Three-dimensional model fields of ocean temperature, and ocean salinity are saved as ten day averages.

As a first observation we note that the changes in the circulation field are gradual so that for the remaining part of the manuscript we will only describe two experiments KPP100 and KPP250, where the name implies the factor by which the background diffusivity coefficient is increased. The resulting background diffusivity coefficients are 5.44×10^{-5} m^2s^{-1} for KPP100 and 1.36×10^{-4} m^2s^{-1} for KPP250.

For a regional sea ice-ocean simulation, the length of spin up period depends on the time of ocean adjustment. In all runs, sea ice concentration develops a reasonable seasonal cycle without obvious spin up drifts after only a few years (Figure 1a). The differences in the mean ocean temperature of the upper 200 m between the sensitivity runs and the baseline run are stable after 2003 (Figure 1b). No obvious ocean drift appeared in the sensitivity runs, thus the simulation results from 2004 to 2013 are used for the analysis in this paper.

3. The Baseline Run

This model was tuned against observation in a systematic way to reproduce sea ice extent and drift observations. In this sense the parameter choice of KPP001 is "optimal" (Nguyen et al., 2011). Figure 2 compares the seasonal cycle of sea ice extent of the KPP001 run with the observation derived from the Multisensor Analyzed Sea Ice Extent (MASIE) data. The MASIE data are derived from the daily 4 km sea ice component of the National Ice Center Interactive Multisensor Snow and Ice Mapping System product and are available from the beginning of 2006. Generally, the KPP001 run simulates lower sea ice extent than the observation. The sea ice extent difference between the KPP001 run and the observation is approximately 1~2 million km^2. Our model does not represent the sea ice edge accurately (not shown), which may contribute to the sea ice extent differences, but the amplitude of sea ice extent seasonal cycle in the KPP001 run is similar to the observation, and the minimum sea ice extent in summer of 2007 and 2012 are also simulated accurately. There is a systematic bias in magnitude and a phase error in the model. The phase error may be attributed to the zero-layer thermodynamics of the sea ice model (Semtner, 1976)

The ocean realism of the KPP001 run is evaluated against hydrographical data from the World Ocean Atlas 2013 (WOA13 V2; Locarnini et al., 2013; Zweng et al., 2013) along the prime meridian from the Atlantic to the Pacific sector (Figure 3) and in the Canadian Basin and Eurasian Basin (Figure 4). Objectively analyzed temperature and salinity climatological fields at 1°-resolution representative for 2005 to 2012 in the WOA13 V2 dataset are compared to model average over the years 2005 to 2012. On the basin scale our model successfully captures the structure of the cold halocline layer in the Canadian Basin and the deep convection feature in the Greenland Sea (Figure 3a, 3c, 3e, 3g). In summertime, our model simulates a warmer temperature core at 400 m depth in the Norwegian Sea (Figure 3b). The warm bias is larger in wintertime (Figure 3d). In the Greenland Sea our model generates a colder upper ocean until 700 m depth in summertime, and the cold anomaly shrinks in wintertime. Around Fram Strait the simulated ocean temperature is higher than the WOA13 V2 data in summertime with maximum bias up to 2 °C spreading from 300 m to 700 m depth. In wintertime the warm bias core moves upwards to the upper ocean and increases to 4 °C in the surface layer. In the Canadian Basin our model produces a slightly warmer surface down to 100 m depth and a moderately colder upper ocean between 100 m and 600 m depth. On the basin scale our model simulates a fresher Arctic Ocean both in summertime and wintertime (Figure 3f, 3h). The maximum fresh bias is in the cold halocline layer of the Canadian Basin with values up to -1.6. Saline anomalies appear in the Beaufort Sea in wintertime.

From the annual mean vertical temperature and salinity distributions in the Canadian Basin and Eurasian Basin (Figure 4), the model simulates a thermal inversion layer in the cold halocline layer where temperature decreases with depth. A warm core appears at 50 m depth in the cold halocline layer. This thermal inversion layer can be found in the 1978 observations of the Polar Science Center Hydrographic Climatology data (See Figure 3b in Zhang and Steele 2007), but not in the WOA13 V2 data. The model produces higher temperature than the WOA13 V2 data in the cold halocline layer and lower Atlantic Water layer, while lower temperature than the WOA13 V2 data in the upper Atlantic Water layer (Figure 4a). The model simulates a fresher upper ocean than the WOA13 V2 data, but the vertical salinity gradient is close to the observations. Although relatively large temperature biases exist in the Greenland Sea, temperature and salinity biases are small in the Arctic deep basin areas where the background diffusion is the dominant mixing process in the model.

4. Sea Ice Response To Increased Vertical Mixing

The sea ice responds to increased vertical mixing in the Arctic Ocean with a perennial reduction of sea ice thickness (Figure 5b) and a notable summertime sea ice concentration decrease (Figure 5a). Compared with the KPP001 run, the September minimum sea ice concentration of the KPP250 is smaller by 5% while the April mean sea ice concentration is only smaller by less than 2%. The basin mean sea ice thickness of the KPP250 is smaller by more than 0.1 m in both summer and wintertime. The April sea ice extent reduces by 0.58% in the KPP100 run and 1.92% in the KPP250 run, while the September sea ice extent decreases by 15.89% in the KPP100 run and 28.48% in the KPP250 run (not shown).

The wintertime sea ice concentration changes mainly along the sea ice edge in the Greenland Sea and Barents Sea (Figure 6a, 6b). In the KPP100 run, sea ice concentration decreases along the sea ice edge in the northern Greenland Sea and Barents Sea, but the exported “ice tongue” along the coast of Greenland extends further eastwards into the southern Greenland Sea (Figure 6a). In the KPP250 run, the extra sea ice area in the southern Greenland Sea is smaller, but the sea ice concentration reduction in the Barents Sea and northern Greenland Sea are much larger (Figure 6b). In summertime the sea ice concentration is smaller both along the sea ice edge and in the pack ice area (Figure 6c, 6d). The sea ice concentration decreases strongly in the northern Greenland Sea, north of Svalbard and in the southern Canadian Basin. The sea ice thickness changes due to stronger vertical mixing are found in the multiyear sea ice region near the Canadian Arctic Archipelago (Figure 7b, 7d). Sea ice thickness decreases more in summertime than in wintertime.

The length of the sea ice season, which is defined as the number of days per year when sea ice concentration is larger than 15%, can be used to characterize the local sea ice conditions (Parkinson et al., 1999; Meier et al., 2007; Cavalieri and Parkinson, 2012). In the KPP001 run, both in the deep basins and in the northwestern Greenland Sea, the length of the sea ice season is longer than 330 days. In the marginal seas along the American and Eurasian continent, the length of the sea ice season is between 200 and 300 days and shorter in the Barents Sea (not shown). In the KPP100 run, the length of the sea ice season decreases in the northern Greenland Sea and the marginal seas of the Eurasian continent, while it increases in the southern Greenland Sea (Figure 7e). In the KPP250 run, the length of the sea ice season further reduces in the Greenland Sea, Barents Sea and the northern part of the East Siberia Sea (Figure

7f).

5. Ocean Responses To Increased Vertical Mixing

In our sensitivity runs, atmospheric forcing data remains the same, so sea ice conditions in the pack ice areas are mainly affected by the underlying ocean state, while sea ice conditions in the sea ice edge areas are also controlled by horizontal heat advection associated with surface ocean currents. Vertical distribution of horizontally averaged ocean temperature, salinity and normalized domain integrated topostrophy are shown in Figure 8. The averaging domain used in the calculation covers areas in the Canadian Basin and Eurasian Basin where total depth is larger than 1000 m. Topostrophy (Holloway et al., 2007) is a scalar expressed by the upwards component of the vector product of velocity (V) and gradient of the total depth (∇D) $V \times \nabla D$. In the northern hemisphere, positive (negative) topostrophy corresponds to flow with shallower water to the right (left). Therefore in the Arctic Ocean, positive (negative) topostrophy represent flows dominated by cyclonic (anti-cyclonic) circulation along steep topography.

5.1 Ocean Temperature and Salinity

In the KPP001 run, the thermal inversion layer locates between 50 m and 120 m depth, a warm core appears at 50 m depth. Warmest water locates between 400 m and 600 m depth in the Atlantic Water layer. In the KPP100 run, the thermal inversion layer and warm core in the cold halocline layer has disappeared. With increasing background diffusivity coefficient, the entire cold halocline layer and Atlantic Water layer become colder, and the location with maximum temperature deepens (Figure 8a).

The surface ocean temperature in the ice covered areas is nearly unaffected by the different diffusivity coefficients, because it is close to the local freezing point (Figure 9a, 9b). SST decreases by 1 °C in the deep convection area of the Greenland Sea, while SST in Fram Strait increases by more than 1 °C in the KPP100 run (Figure 9a). In the KPP250 run, the warm SST bias area in Fram Strait expands and the cold SST bias area in the Greenland Sea shrinks. SST in the Baffin Bay and Beaufort Sea are getting colder when the vertical mixing increases (Figure 9b).

At 200 m depth, approximately the bottom of the cold halocline layer, the mean ocean temperature decreases with increasing diffusivity (Figure 8a). In the KPP100 run, ocean temperature decreases by 1 °C in the Baffin Bay and Canadian Arctic Archipelago, and decreases by 1.5 °C in the western Greenland Sea (Figure 9c). The largest ocean temperature reduction of up to -2 °C appears in the southern Eurasian Basin. Ocean temperature in the western Norwegian Sea increases by 2 °C and the area north of Fram Strait also becomes warmer. In the KPP250 run, excessive ocean temperature reduction up to -2 °C occurs in the western Greenland Sea, Baffin Bay and southern Eurasian Basin (Figure 9d). Below the Atlantic Water layer, ocean temperature at 1200 m depth also decreases slightly, but mainly in the Eurasian Basin (Figure 9e, 9f).

The vertical distribution of ocean salinity in the Arctic Ocean determines the strength of the cold halocline layer as well as the upper ocean stratification. In the KPP001 run, the mean salinity at the ocean surface is lower than 30.5 and increases to 34 at 200 m depth. When vertical mixing increases, the vertical salinity gradient of the cold halocline layer reduces and the Atlantic Water layer becomes fresher. More saline water has entered into deep ocean below the Atlantic Water layer (Figure 8b). Surface water in the Canadian Basin and the East Siberia Sea and Laptev Sea area are much fresher than other areas in the KPP001 run (not shown). The fresh water in the Canadian Basin is a result of summer sea ice melting processes while the fresh water in the East Siberia Sea and Laptev Sea area is mainly river runoff from Russia. In the KPP100 run, surface water becomes more saline in the Canadian Basin and fresher in the East Siberia Sea and Laptev Sea area (Figure 10a). In the KPP250 run, the whole surface layer of the Arctic Basin is covered by more saline water except for the East Siberia Sea and Laptev Sea area where fresh river discharge on the shelf is not affected by interior vertical background mixing (Figure 10b). At the bottom of the cold halocline layer, the water is fresher with more vertical mixing by up to -2 in the whole Arctic Basin (Figure 10c, 10d). Below the Atlantic Water layer, saline water covers the whole Canadian Basin (Figure 10e, 10f).

5.2 Ocean Circulation

Observations show that the Atlantic Water enters the Arctic Ocean with the West Spitsbergen Current in the eastern part Fram Strait, subducts north of the Svalbard Islands and flows as a rim current cyclonically around the boundary of the Arctic basin (Rudels et al., 1994; Woodgate et al., 2001; Lenn et al., 2009). Simulating this circulation is challenging and only half of the models in the Arctic Ocean Model

Intercomparison Project (AOMIP) were able to correctly simulate the cyclonic Atlantic Water layer circulation (Yang, 2005). In the KPP001 run, cyclonic circulation pattern dominates the Atlantic Water layer in the Canadian Basin and Eurasian Basin. The “strongest” cyclonic circulation is at 350 m depth. When vertical mixing increases, the cyclonic circulation increases in the surface ocean shallower than 20 m depth and in the interior ocean deeper than 750 m depth, but decreases between these layers (measured by topostrophy in Figure 8c).

In the surface layer, the Norwegian Atlantic Current flows along the coast of Norway, then splits into the West Spitsbergen Current and the North Cape Current at around 75 °N in the KPP001 run. The West Spitsbergen Current flows northwestward into Fram Strait partly feeding the East Greenland Current and Atlantic current recirculation. The North Cape Current flows in the marginal seas of the Eurasian continent until the Laptev Sea. The Beaufort Gyre is partly fed by currents along the coast of Canadian Arctic Archipelago which originated from the West Spitsbergen Current, and partly fed by currents from the Bering Strait. A northward current occurs along the western Baffin Bay after passing through the Canadian Arctic Archipelago (Figure 11a). In the KPP250 run, anomalous westward flow occurs along the eastern edge of the Canadian Basin and Eurasian Basin. Further, there is anomalous flow from the North Pole toward Greenland, where it turns westward into Fram Strait. The Atlantic current recirculation in the Greenland Sea weakens (Figure 11b).

At 200 m depth, the East Greenland Current, West Spitsbergen Current and Atlantic current recirculation constitute the main flow pattern in the Greenland Sea. The Arctic Circumpolar Current is obvious in the KPP001 run (Figure 11c). In the KPP250 run, the Beaufort Gyre is stronger. Anomalous westward flows occur along the edge of the Eurasian continent and Canadian Arctic Archipelago. The Atlantic current recirculation in the Greenland Sea also becomes weaker (Figure 11d). At 750 m depth, cyclonic circulation anomalies appear at the eastern Makarov Basin while anti-cyclonic circulation anomalies occur in the Greenland Sea (Figure 11f).

6. Tracer tendency terms as proxy for vertical fluxes

To describe the effect of vertical background diffusivity in our experiments in a more quantitative way, we compare tracer tendencies due to vertical background diffusivity with those due to vertical advection (Figure 12).

The vertical background diffusivity tracer tendency terms are

$$\frac{\partial T}{\partial t_{bd}} = -\frac{\partial}{\partial z}\left(-K_{bd}\frac{\partial T}{\partial z}\right), \quad \frac{\partial S}{\partial t_{bd}} = -\frac{\partial}{\partial z}\left(-K_{bd}\frac{\partial S}{\partial z}\right),$$

and the vertical advection tracer tendency terms are

$$\frac{\partial T}{\partial t_{va}} = -w\frac{\partial T}{\partial z}, \frac{\partial S}{\partial t_{va}} = -w\frac{\partial S}{\partial z},$$

where T, S represent temperature and salinity, K_{bd} is vertical background diffusivity coefficient, z is depth, w is vertical velocity.

In the KPP001 run, $\frac{\partial T}{\partial t_{bd}}$ has the same magnitude as $\frac{\partial T}{\partial t_{va}}$ (Figure 12a, 12b), and the vertical background diffusivity contribution to the vertical heat exchange in the Atlantic Water layer and lower cold halocline layer is small. When K_{bd} is increased, $\frac{\partial T}{\partial t_{bd}}$ becomes more important than $\frac{\partial T}{\partial t_{va}}$ in the vertical heat exchange. The vertical background diffusivity cools the Atlantic Water layer and lower cold halocline layer in the KPP100 run. In the Atlantic Water layer, this "cooling" effect increases with increasing K_{bd}.

In the KPP001 run, $\frac{\partial S}{\partial t_{bd}}$ is smaller than $\frac{\partial S}{\partial t_{va}}$ in generating the vertical salinity distribution (Figure 12c, 12d). $\frac{\partial S}{\partial t_{bd}}$ increases with K_{bd}, but $\frac{\partial S}{\partial t_{va}}$ becomes smaller. Increasing the vertical background diffusivity increases salinity in the surface layer and decreases salinity in the lower cold halocline layer. In the Atlantic Water layer, $\frac{\partial S}{\partial t_{bd}}$ of the KPP250 run is smaller than that of the KPP100 run, which implies that increasing of K_{bd} leads to decreasing Atlantic Water layer salinity.

7. Discussion and Conclusion

In this paper, the Arctic Ocean and sea ice response to increased vertical mixing are investigated based on a sea ice-ocean model. It is found that increased vertical mixing reduces sea ice thickness all year round and decreases summertime sea ice concentration. The sea ice thickness reduction occurs in areas with thick multiyear sea ice near the Canadian Arctic Archipelago while summertime sea ice concentration decreases both in the marginal sea ice zone and in the pack.

In thick multiyear sea ice zone near the Canadian Arctic Archipelago, the sea ice concentration is almost equal to one and there are only very few sea ice leads and zones of open water. As a consequence, the upward heat flux in the surface ocean layer can be used almost entirely to melt sea ice. In marginal sea ice zone with more sea ice leads and more open water, a large part of the upward heat flux in surface ocean layer will be released to atmosphere. Therefore with increased vertical background diffusivity, substantial sea ice thickness reduction occurs in areas with thick multiyear sea ice zone near the Canadian Arctic Archipelago, but not so much in the marginal ice zone. In the pack ice zone, sea ice concentration and thickness in summertime is distinctly lower than in wintertime. The upward ocean heat flux is overruled by a stronger downward atmospheric heat flux in the cold season, while in summertime with warmer atmospheric temperatures, the upward heat flux can melt the ice both vertically and laterally. Thus summertime sea ice concentration decreases both in the marginal sea ice zone and in the pack, while wintertime sea ice concentration decreases mostly in the marginal sea ice zone.

In the Canadian and Eurasian Basin, the increased vertical mixing will speed up vertical heat and salinity exchange, bring the underlying warm and saline water into the surface layer to melt sea ice, and induce cooling of the cold halocline layer and the Atlantic Water layer. The strength of the cold halocline layer weakens together with a much fresher Atlantic Water layer, and more volume of saline water enters into deep ocean below the Atlantic Water layer. In the surface layer, water becomes more saline in the Canadian Basin, but fresher in the East Siberian Sea and Laptev Sea areas. This difference may be due to external freshwater forcing. In the Canadian Basin, there is little external freshwater forcing, and increased vertical mixing induces excessive mixing in the surface layer and the cold halocline layer, thus surface water becomes more saline. In the Laptev Sea, strong river runoff continuously inputs freshwater into the Laptev Sea and increased vertical mixing perturbs the upper 80 m of the water column (not shown), so that the surface water becomes fresher in the Laptev Sea. At 200 m depth, strong ocean temperature reductions by up to 2 °C appear in the western Greenland Sea, Baffin Bay and southern Eurasian Basin. The result of stronger vertical mixing leads to more heat escaping from the Atlantic Water layer into the surface layer. A cooling of the Atlantic Water layer is also reported in Zhang and Steele (2007).

The increased vertical mixing induces cyclonic circulation anomalies in the surface layer shallower than 20 m depth and in the interior ocean deeper than 700 m depth, but anti-cyclonic circulation anomalies between them. At the surface layer, there is an anomalous westward surface flow along the eastern edge of the Canadian Basin and the Eurasian Basin. The Atlantic current recirculation in the Greenland Sea weakens with increased vertical mixing. At 200 m depth, the Beaufort Gyre accelerates. There is anomalous westward flow along the edge of the Eurasian continent and the Canadian Arctic Archipelago. At 750 m depth, cyclonic circulation anomalies appear in the eastern Makarov Basin while there are anti-cyclonic circulation anomalies in the Greenland Sea. Anti-cyclonic circulation anomalies mean that the basic cyclonic circulation decelerates and less heat, which is carried by the cyclonic circulation, enters the Canadian Basin and the Eurasian Basin. The heat decrements corresponding to the anti-cyclonic circulation anomalies may partly contribute to cooling of the Eurasian Basin at 200 m depth. Zhang and Steele (2007) found that excessively strong vertical mixing (approximately 1.25×10^{-4} m^2s^{-1}) changes the basic cyclonic Atlantic layer circulation pattern into an anticyclonic pattern in the Canadian Basin. In this study, excessively strong vertical mixing (approximately 1.36×10^{-4} m^2s^{-1}) does not change the basic cyclonic Atlantic layer circulation pattern in the Canadian Basin. This difference may be partly due to the different models used by the two studies. Different models implement different physical parameterizations, so that they simulate different upper ocean properties and stratification. The same increments of vertical mixing coefficient may induce different stratification changes, which further lead to different Atlantic layer circulation patterns.

Corroborating our findings from the viewpoint of decreased vertical mixing, previous studies also found that stronger Arctic Ocean stratification due to increased freshwater input leads to a warming of the cold halocline layer and Atlantic Water layer, and an accelerating of the cyclonic circulation in Atlantic Water layer (Nummelin et al., 2016). In the context of global warming (Hartmann et al., 2013) and with the Arctic summer sea ice cover decline (Stroeve et al., 2005, 2008), the vertical mixing in the interior Arctic Ocean will likely increase (see Guthrie et al., 2013 for an alternative point of view). The increased vertical mixing will speed up vertical heat and salinity exchange, the decreased vertical temperature and salinity gradient of the upper Arctic ocean leads to a weaker Arctic Ocean stratification with consequences for the circulation pattern. The heat of the Atlantic Water layer will eventually reach the surface layer and contribute to melting the sea ice. This mechanism is also partly supported by Zhang et al. (2000), where the increased input of Atlantic water into Arctic Ocean and reduced halocline strength (Steele and Boyd, 1998) cause an increased upward heat flux, which limits ice growth and enhances lateral melting. Considering such physical mechanisms, the Arctic Ocean may become ice free in summer earlier than predicted by current climate models with prescribed constant vertical background diffusivity.

Temperature and salinity biases exist between the baseline run and WOA13 data. These biases have a negligible effect on our conclusion. First, the WOA13 data themselves are biased towards summer conditions when it is easier to collect observations in the Arctic Ocean. Second, when analyzing model results we describe the differences between the sensitivity runs and the baseline run, these differences are almost independent of the biases. Third, our study can be seen as a qualitative research in the sense that the conclusion of the study, that is, increased vertical mixing reduces sea ice thickness and the vertical salinity gradient of the cold halocline layer, will not change even if the biases amplify. So far, our study has shown that the vertical mixing induces extra heat and salinity exchange that will have a noticeable impact on the upper ocean structure, ocean circulation and sea ice in the Arctic ocean. However, the design of our experiments with modified constant background diffusivity coefficient may be too simple to do justice to complex interplay of processes in the interior Arctic. A more sophisticated mixing scheme for Arctic model may be necessary to corroborate our results. It is difficult to estimate a threshold value for vertical background mixing for which the response of the Arctic circulation and sea ice will be significant. Additionally, in our experiment the vertical mixing of the entire water column was increased, whereas in a more realistic scenario, wind-driven mixing mostly occurs in upper several hundred meters and tide-driven mixing occurs around rough topography. In this sense, our results may serve as an early step towards exploring the effects of vertical mixing in a changing Arctic Ocean.

Acknowledgments. The authors thank the National Snow and Ice Data Center (NSIDC) for providing the MASIE data (http://nsidc.org/data/masie/), the National Oceanic and Atmospheric Administration (NOAA) for the WOA13 V2 data (https://www.nodc.noaa.gov/OC5/woa13/woa13data.html), the Japan Meteorological Agency (JMA) for the JRA analysis data (http://jra.kishou.go.jp/JRA-55/index_en.html). We thank An T. Nguyen for providing the model configuration. We thank the two anonymous reviewers for the constructive comments. This work is supported by the National Natural Science Foundation of China (41506224). This paper is a contribution to the project T3 (Energy transfers in gravity plumes) of the Collaborative Research Centre TRR 181 “Energy Transfer in Atmosphere and Ocean” funded by the German Research Foundation.

References and Citations

Althaus, A. M., E. Kunze, and T. B. Sanford (2003), Internal tide radiation from Mendocino Escarpment, *J. Phys. Oceanogr.,* 33, 1510–1527, doi:10.1175/1520-0485.

Antonov, J. I., R. A. Locarnini, T. P. Boyer, A. V. Mishonov, and H. E. Garcia (2006), World Ocean Atlas 2005, Volume 2: Salinity. S. Levitus, Ed. NOAA Atlas NESDIS 62, U.S. Government Printing Office, Washington, D.C., 182 pp.

Bintanja, R., and F. M. Selten (2014), Future increases in Arctic precipitation linked to local evaporation and sea-ice retreat. *Nature,* 509(7501), 479-482.

Carter, G. S., and M. C. Gregg (2002), Intense variable mixing near the head of Monterey Submarine Canyon, *J. Phys. Oceanogr.,* 32, 3145–3165, doi:10.1175/1520-0485.

Cavalieri, D. J., and C. L. Parkinson (2012), Arctic sea ice variability and trends, 1979–2010, *Cryosphere*., 6, 881–889, doi:10.5194/tc-6-881-2012.

Comiso, J. C., C. L. Parkinson, R. Gersten, and L. Stock (2008), Accelerated decline in the Arctic sea ice cover. *Geophys. Res. Lett.,* 35, L01703, http://dx.doi.org/10.1029/2007GL031972.

Davis, P. E. D., C. Lique, H. L. Johnson, and J. D. Guthrie (2016), Competing effects of elevated vertical mixing and increased freshwater input on the stratification and sea ice cover in a changing Arctic Ocean, *J. Phys. Oceanogr.,* 46, 1531–1553, doi:10.1175/Jpo-D-15-0174.1.

Fer, I. (2009), Weak vertical diffusion allows maintenance of cold halocline in the central Arctic. *Atmos. Oceanic Sci. Lett.,* 2(3), 148–152.

Fer, I., R. Skogseth, and F. Geyer (2010), Internal waves and mixing in the marginal ice zone near the Yermak Plateau, *J. Phys. Oceanogr.,* 40(7), 1613–1630, doi:10.1175/2010JPO4371.1.

Ferrari, R., and C. Wunsch (2009), Ocean circulation kinetic energy: Reservoirs, sources, and sinks. *Annu. Rev. Fluid. Mech.,* 41, 253–282, http://dx.doi.org/10.1146/annurev.fluid.40.111406.102139.

Gao, Y., J. Sun, F. Li, S. He, S. Sandven, Q. Yan, Z. Zhang, K. Lohmann, N. Keenlyside, T. Furevik, and L. Suo (2015), Arctic sea ice and Eurasian climate: A review, *Adv. Atmos. Sci.,* 32(1), 92-114.

Goosse, H., E. Deleersnijder, T. Fichefet, and M. H. England (1999), Sensitivity of a global coupled ocean-sea ice model to the parameterization of vertical mixing. *J.*

Geophys. Res. Oceans., 104(C6), 13681–13695.

Gregg, M. C. (1987), Diapycnal mixing in the thermocline: A review, *J. Geophys. Res.,* 92, 5249–5286, doi:10.1029/JC092iC05p05249.

Guthrie, J. D., J. H. Morison, and I. Fer (2013), Revisiting internal waves and mixing in the Arctic Ocean. *J. Geophys. Res. Oceans,* 118, 3966-3977, doi: 10.1002/jgrc.20294.

Harada, Y., H. Kamahori, C. Kobayashi, H. Endo, S. Kobayashi, Y. Ota, H. Onoda, K. Onogi, K. Miyaoka, and K. Takahashi (2016), The JRA-55 Reanalysis: Representation of atmospheric circulation and climate variability, *J. Meteor. Soc. Japan.*, 94, 269-302, doi:10.2151/jmsj.2016-015.

Hartmann, D. L., A. M. G. Klein Tank, and M. Rusticucci (2013). "Observations: Atmosphere and Surface". IPCC WGI AR5 (Report). p. 198.

Holloway, G., F. Dupont, E. Golubeva, S. Häkkinen, E. Hunke, M. Jin, M. Karcher, F. Kauker, M. Maltrud, M. A. Morales Maqueda, W. Maslowski, G. Platov, D. Stark, M. Steele, T. Suzuki, J. Wang, and J. Zhang (2007), Water properties and circulation in arctic ocean models. *J. Geophys. Res. Oceans.,* 112(C4), 225-237.

Jensen, M. F., J. Nilsson, and K. H. Nisancioglu (2016), The interaction between sea ice and salinity-dominated ocean circulation: implications for halocline stability and rapid changes of sea ice cover. *Clim Dynam.,* 47(9-10), 1-17.

Jing, Z., L. Wu, L. Li, C. Liu, X. Liang, Z. Chen, D. Hu, and Q. Liu (2011), Turbulent diapycnal mixing in the subtropical northwestern Pacific: Spatial-seasonal variations and role of eddies, *J. Geophys. Res.,* 116, C10028, doi:10.1029/2011JC007142.

Klymak, J. M., J. N. Moum, J. D. Nash, E. Kunze, J. B. Girton, G. S. Carter, C. M. Lee, T. B. Sanford, and M. C. Gregg (2006), An estimate of tidal energy lost to turbulence at the Hawaiian Ridge, *J. Phys. Oceanogr.,* 36, 1148–1164, doi:10.1175/JPO2885.1.

Kobayashi, S., Y. Ota, Y. Harada, A. Ebita, M. Moriya, H. Onoda, K. Onogi, H. Kamahori, C. Kobayashi, H. Endo, K. Miyaoka, and K. Takahashi (2015), The JRA-55 Reanalysis: General specifications and basic characteristics. *J. Meteor. Soc. Japan.*, 93, 5-48, doi:10.2151/jmsj.2015-001.

Kunze, E., and J. M. Toole (1997), Tidally driven vorticity, diurnal shear, and turbulence atop Fieberling Seamount, *J. Phys. Oceanogr.,* 27,2663–2693, doi:10.1175/1520-0485.

Kunze, E., E. Firing, J. M. Hummon, T. K. Chereskin, and A. M. Thurnherr (2006), Global abyssal mixing inferred from lowered ADCP shear and CTD strain profiles, *J. Phys. Oceanogr.,* 36, 1553–1576, doi:10.1175/JPO2926.1.

Large, W. G., J. C. McWilliams, and S. C. Doney (1994), Oceanic vertical mixing:A review and a model with a nonlocal boundary layer parameterization. *Rev. Geophys.,* 32, 363-403.

Lenn, Y. D., P. J. Wiles, S. Torres‐Valdes, E. P. Abrahamsen, T. P. Rippeth, J. H. Simpson, S. Bacon, S. W. Laxon, I. Polyakov, V. Ivanov, and S. Kirillov (2009), Vertical mixing at intermediate depths in the arctic boundary current. *Geophys. Res. Lett.,* 36, L05601, doi:10.1029/2008GL036792.

Locarnini, R. A., A. V. Mishonov, J. I. Antonov, T. P. Boyer, and H. E. Garcia (2006), World Ocean Atlas 2005, Volume 1: Temperature. S. Levitus, Ed. NOAA Atlas NESDIS 61, U.S. Government Printing Office, Washington, D.C., 182 pp.

Locarnini, R. A., A. V. Mishonov, J. I. Antonov, T. P. Boyer, H. E. Garcia, O. K. Baranova, M. M. Zweng, C. R. Paver, J. R. Reagan, D. R. Johnson, M. Hamilton, and D. Seidov (2013), World Ocean Atlas 2013, Volume 1: Temperature. S. Levitus, Ed., A. Mishonov Technical Ed.; NOAA Atlas NESDIS 73, 40 pp.

Losch, M., D. Menemenlis, J. M. Campin, P. Heimbach, and C. Hill (2010), On the formulation of sea-ice models. Part 1: Effects of different solver implementations and parameterizations. *Ocean Model.,* 33, 129–144.

Lueck, R. G., and T. D. Mudge (1997), Topographically induced mixing around a shallow seamount, *Science*, 276, 1831–1833, doi:10.1126/science.276.5320.1831.

Marshall, J., A. Adcroft, C. Hill, L. Perelman, and C. Heisey (1997), A finite-volume, incompressible Navier-Stokes model for studies of the ocean on parallel computers. *J. Geophys. Res.,* 102, 5753–5766, doi: 10.1029/96JC02775.

Meier, W. N., J. Stroeve, and F. Fetterer (2007), Whither Arctic sea ice?A clear signal of decline regionally, seasonally and extending beyond the satellite record, *Ann. Glaciol.,* 46, 428–434, doi:10.3189/172756407782871170.

Menemenlis, D., J. M. Campin, P. Heimbach, C. Hill, T. Lee, A. Nguyen, M. Schodlok, and H. Zhang (2008), ECCO2: High resolution global ocean and sea ice data synthesis, *Mercator Ocean Q. Newsl.,* 31, 13–21.

Nguyen, A. T., D. Menemenlis, and R. Kwok (2011), Arctic ice-ocean simulation with optimized model parameters: Approach and assessment, *J. Geophys. Res.,* 116, C04025, doi:10.1029/2010JC006573.

Nummelin, A., M. Ilicak, C. Li, and L. H. Smedsrud (2016), Consequences of future increased Arctic runoff on Arctic Ocean stratification, circulation, and sea ice cover, *J. Geophys. Res. Oceans*, 121, 617–637, doi:10.1002/2015JC011156.

Onogi, K., J. Tsutsui, H. Koide, M. Sakamoto, S. Kobayashi, H. Hatsushika, T. Matsumoto, N. Yamazaki, H. Kamahori, K. Takahashi, S. Kadokura, K. Wada, K. Kato, R. Oyama, T. Ose, N. Mannoji and R. Taira (2007), The JRA-25 Reanalysis. *J. Meteor. Soc. Japan,* 85, 369-432.

Parkinson, C. L., and D. J. Cavalieri (2008), Arctic sea ice variability and trends, 1979–2006, *J. Geophys. Res.,* 113, C07003, doi:10.1029/2007JC004558.

Parkinson, C. L., D. J. Cavalieri, P. Gloersen, H. J. Zwally, and J. C. Comiso (1999), Arctic sea ice extents, areas, and trends, 1978–1996, *J. Geophys. Res.,* 104(C9), 20,837–20,856, doi:10.1029/1999JC900082.

Perovich, D.K. (2011), The changing Arctic sea ice cover. *Oceanography,* 24(3), 162–173, http://dx.doi.org/10.5670/oceanog.2011.68.

Rudels, B., E. P. Jones, L. G. Anderson, and G. Kattner (1994), On the intermediate depth waters of the Arctic Ocean, in The Polar Oceans and Their Role in Shaping the Global Environment, edited by O. M. Johannessen, R. D. Muench, and J. E. Overland, pp. 33– 46, AGU, Washington, D. C.

Semtner, A. J. J. (1976). A model for the thermodynamic growth of sea ice in numerical investigations of climate. *J. Phys. Oceanogr.,* 6(3), 379-389.

Simmons, H. L., R. W. Hallberg, and B. K. Arbic (2004), Internal wave generation in a global baroclinic tide model, *Deep Sea Res., Part II,* 51, 3043-3068.

Smith, W. H. F., and D. T. Sandwell (1997), Global sea floor topography from satellite altimetry and ship depth soundings. *Science*, 277(5334), 1956–1962, doi: 10.1126/science.277.5334.1956.

St. Laurent, L. C., J. M. Toole, and R. W. Schmitt (2001), Buoyancy forcing by turbulence above rough topography in the abyssal basin, *J. Phys. Oceanogr.,* 31, 3476–3495, doi:10.1175/1520-0485.

St. Laurent, L. C., H. L. Simmons, and S. R. Jayne (2002), Estimating tidally driven mixing in the deep ocean, *Geophys. Res. Lett.,* 29(23),2106, doi: 10.1029/2002GL015633.

Steele, M., and T. Boyd (1998), Retreat of the cold halocline layer in the Arctic Ocean, *J. Geophys. Res.,* 103, 10,419– 10,435.

Stroeve, J., M. Serreze, S. Drobot, S. Gearheard, M. Holland, J. Maslanik, W. Meier, and T. Scambos (2008), Arctic sea ice extent plummets in 2007, EOS Trans., AGU, 89(2), 13–14.

Stroeve, J. C., M. C. Serreze, F. Fetterer, T. Arbetter, W. Meier, J. Maslanik, and K. Knowles (2005), Tracking the Arctic's shrinking ice cover: Another extreme September minimum in 2004, *Geophys. Res. Lett.,* 32, L04501, doi:10.1029/2004GL021810.

Turner, J. S. (2010), The melting of ice in the Arctic Ocean: The influence of double-diffusive transport of heat from below, *J. Phys. Oceanogr.,* 40(1), 249–256, doi:10.1175/2009JPO4279.1.

Woodgate, R. A., K. Aagaard, R. D. Muench, J. Gunn, G. Björk, B. Rudels, A. T. Roach, and U. Schauer (2001), The Arctic Ocean Boundary Current along the Eurasian slope and the adjacent Lomonosov Ridge: Water mass properties, transports and transformations from moored instruments, *Deep Sea Res., Part I,* 48(8), 1757– 1792.

Yang, J. (2005), The Arctic and subarctic ocean flux of potential vorticity and the Arctic Ocean circulation, *J. Phys. Oceanogr.,* 35, 2387–2407.

Yang, J., J. Comiso, D. Walsh, R. Krishfield, and S. Honjo (2004), Storm-driven mixing and potential impact on the Arctic Ocean, *J. Geophys. Res.,* 109, C04008, doi:10.1029/2001JC001248.

Zhang, J., D. A. Rothrock, and M. Steele (2000), Recent changes in Arctic sea ice: The interplay between ice dynamics and thermodynamics, *J. Clim.,* 13, 3099-3114.

Zhang, J., and M. Steele (2007), Effect of vertical mixing on the Atlantic Water layer circulation in the Arctic Ocean, *J. Geophys. Res.,* 112, C04S04, doi:10.1029/2006JC003732.

Zweng, M. M, J. R. Reagan, J. I. Antonov, R. A. Locarnini, A. V. Mishonov, T. P. Boyer, H. E. Garcia, O. K. Baranova, D. R. Johnson, D. Seidov, M. M. Biddle (2013), World Ocean Atlas 2013, Volume 2: Salinity. S. Levitus, Ed., A. Mishonov Technical Ed.; NOAA Atlas NESDIS 74, 39 pp.

Figure Captions

Figure 1. Time series of basin mean (a) sea ice concentration and (b) upper 200 m averaged ocean temperature in °C. The black, blue, red curves represent the KPP001, KPP100, KPP250 runs, respectively.

Figure 2. Time series of sea ice extent in km^2. The solid and dashed line represents the KPP001 run and MASIE data.

Figure 3. The 2005-2012 mean ocean temperature in °C and salinity along the prime meridian from Atlantic to Pacific section of the KPP001 control run (1^{st} column), and difference of KPP001 to World Ocean Atlas data (WOA13, 2^{nd} column). The temperature in summertime, temperature in wintertime, salinity in summertime, salinity in wintertime are shown in rows 1 to 4, respectively. Wintertime refers to January, February and March. Summertime refers to July, August and September.

Figure 4. The 2005-2012 mean vertical distributions of spatial averaged (a) ocean temperature in °C and (b) salinity. The domain used in the calculation covers areas in the Canadian Basin and Eurasian Basin where the total depth is larger than 1000 m. The solid and dashed lines represent the KPP001 run and WOA13 data, respectively.

Figure 5. Annual cycle of basin mean (a) sea ice concentration and (b) sea ice thickness in m. The black, blue, red curves represent the KPP001, KPP100, KPP250 runs, respectively.

Figure 6. Differences of the 2004-2013 mean sea ice concentration between runs KPP100 and KPP001 (1^{st} column) and between runs KPP250 and KPP001 (2^{nd} column). Rows 1 to 2 show the April sea ice concentration, the September sea ice concentration.

Figure 7. Differences of the 2004-2013 mean sea ice thickness in m and length of sea ice season in days between runs KPP100 and KPP001 (1^{st} column) and between runs KPP250 and KPP001 (2^{nd} column). Rows 1 to 3 show the April sea ice thickness, the September sea ice thickness, the length of sea ice season.

Figure 8. Vertical distribution of domain mean (a) ocean temperature in °C, (b) ocean salinity, and normalized domain integrated (c) topostrophy. The averaging domain used in the calculation cover areas in the Canadian Basin and Eurasian Basin where total depth is larger than 1000 m. The black, blue, red curves represent the KPP001, KPP100, KPP250 runs, respectively.

Figure 9. Differences in the 2004-2013 mean ocean temperature in °C at different depths between runs KPP100 and KPP001 (1st column) and runs KPP250 and KPP001 (2nd column). Rows 1 to 3 show surface temperature, temperature at 200 m depth, temperature at 1200 m depth.

Figure 10. Difference in the 2004-2013 mean ocean salinity between runs KPP100 and KPP001 (1nd column) and runs KPP250 and KPP001 (2nd column) . Rows 1 to 3 show surface salinity, salinity at 200 m depth, salinity at 2000 m depth.

Figure 11. The 2004-2013 mean ocean current in ms^{-1} (1st column) and difference between runs KPP250 and KPP001 (2nd column). Rows 1 to 3 show velocity at 10 m depth, 200 m depth, 750 m depth. Color denotes the absolute velocity.

Figure 12. Tracer tendency terms in the Canadian Basin and Eurasian Basin. (a) $\frac{\partial T}{\partial t}_{bd}$, (b) $\frac{\partial T}{\partial t}_{va}$, (c) $\frac{\partial S}{\partial t}_{bd}$, (d) $\frac{\partial S}{\partial t}_{va}$. Units for (a) and (b) are **°C***s^{-1}. Units for (c) and (d) are s^{-1}. The black, blue, red curves represent the KPP001, KPP100, KPP250 runs, respectively.

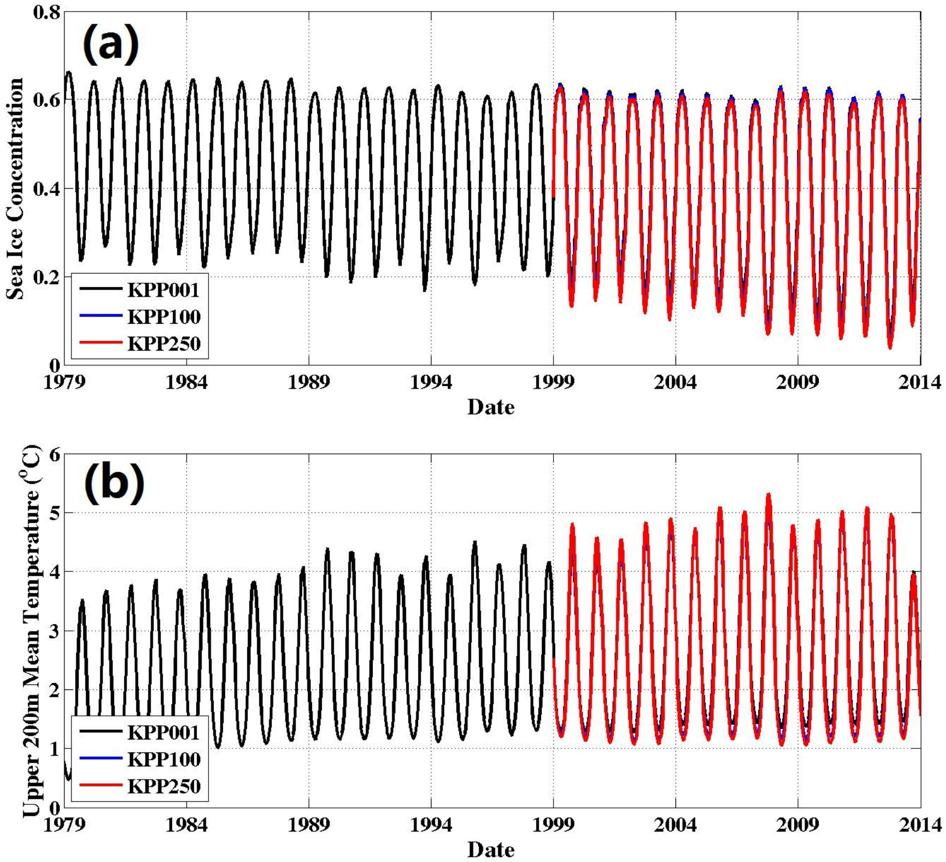

Figure 1. Time series of basin mean (a) sea ice concentration and (b) upper 200 m averaged ocean temperature in °C. The black, blue, red curves represent the KPP001, KPP100, KPP250 runs, respectively.

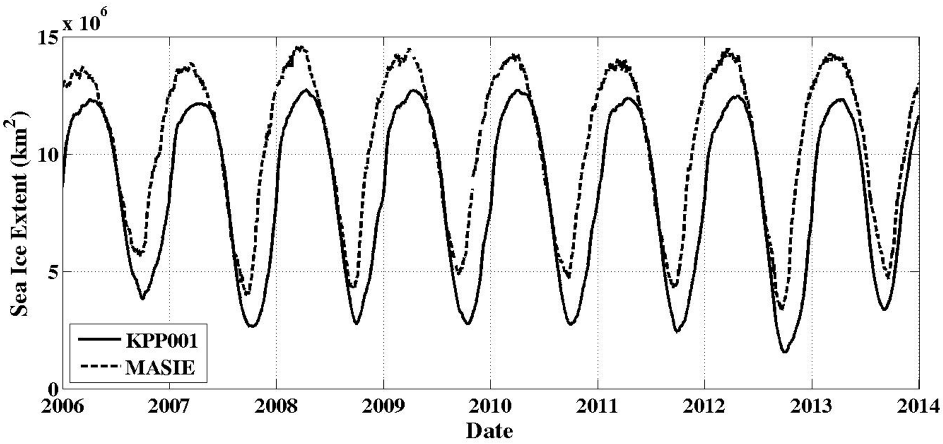

Figure 2. Time series of sea ice extent in km^2. The solid and dashed line represents the KPP001 run and MASIE data, respectively.

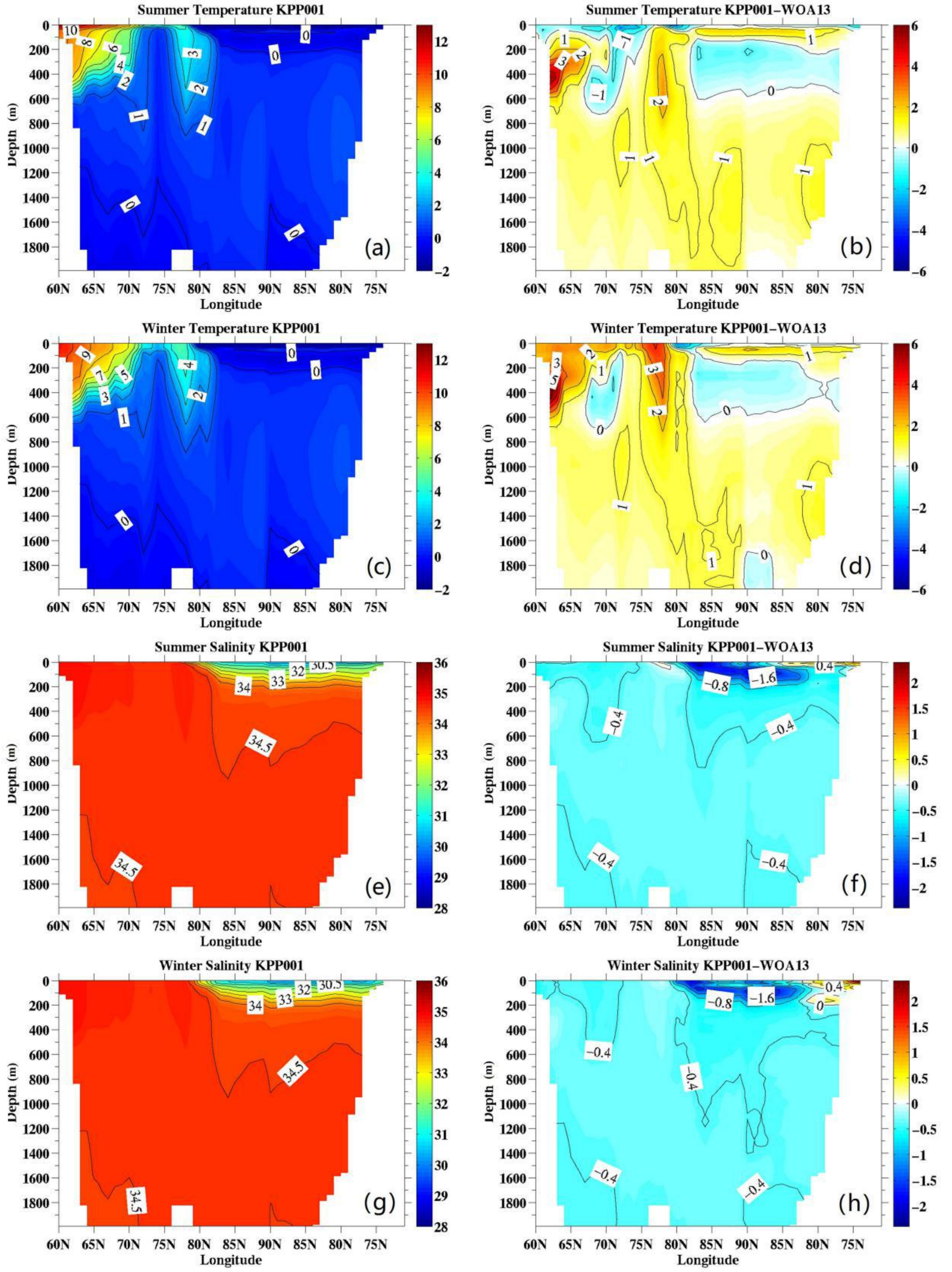

Figure 3. The 2005-2012 mean ocean temperature in °C and salinity along the prime meridian from Atlantic to Pacific section of the KPP001 control run (1st column), and difference of KPP001 to World Ocean Atlas data (WOA13, 2nd column). The temperature in summertime, temperature in wintertime, salinity in summertime, salinity in wintertime are shown in rows 1 to 4, respectively. Wintertime refers to January, February and March. Summertime refers to July, August and September.

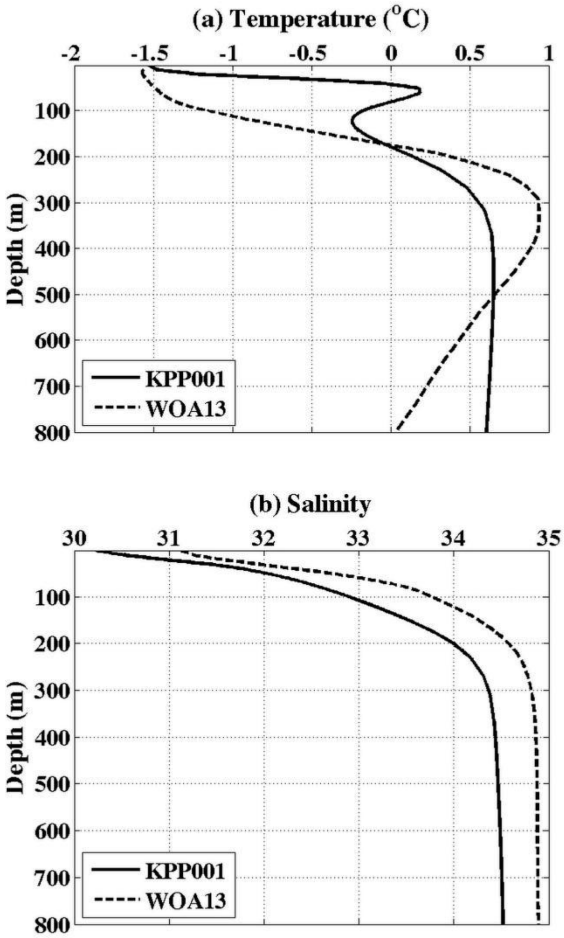

Figure 4. The 2005-2012 mean vertical distributions of spatial averaged (a) ocean temperature in °C and (b) salinity. The domain used in the calculation covers areas in the Canadian Basin and Eurasian Basin where the total depth is larger than 1000 m. The solid and dashed lines represent the KPP001 run and WOA13 data, respectively.

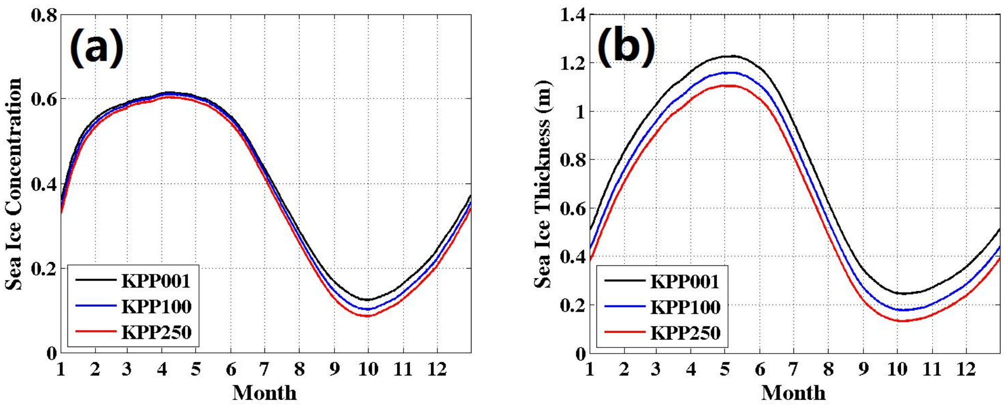

Figure 5. Annual cycle of basin mean (a) sea ice concentration and (b) sea ice thickness in m. The black, blue, red curves represent the KPP001, KPP100, KPP250 runs, respectively.

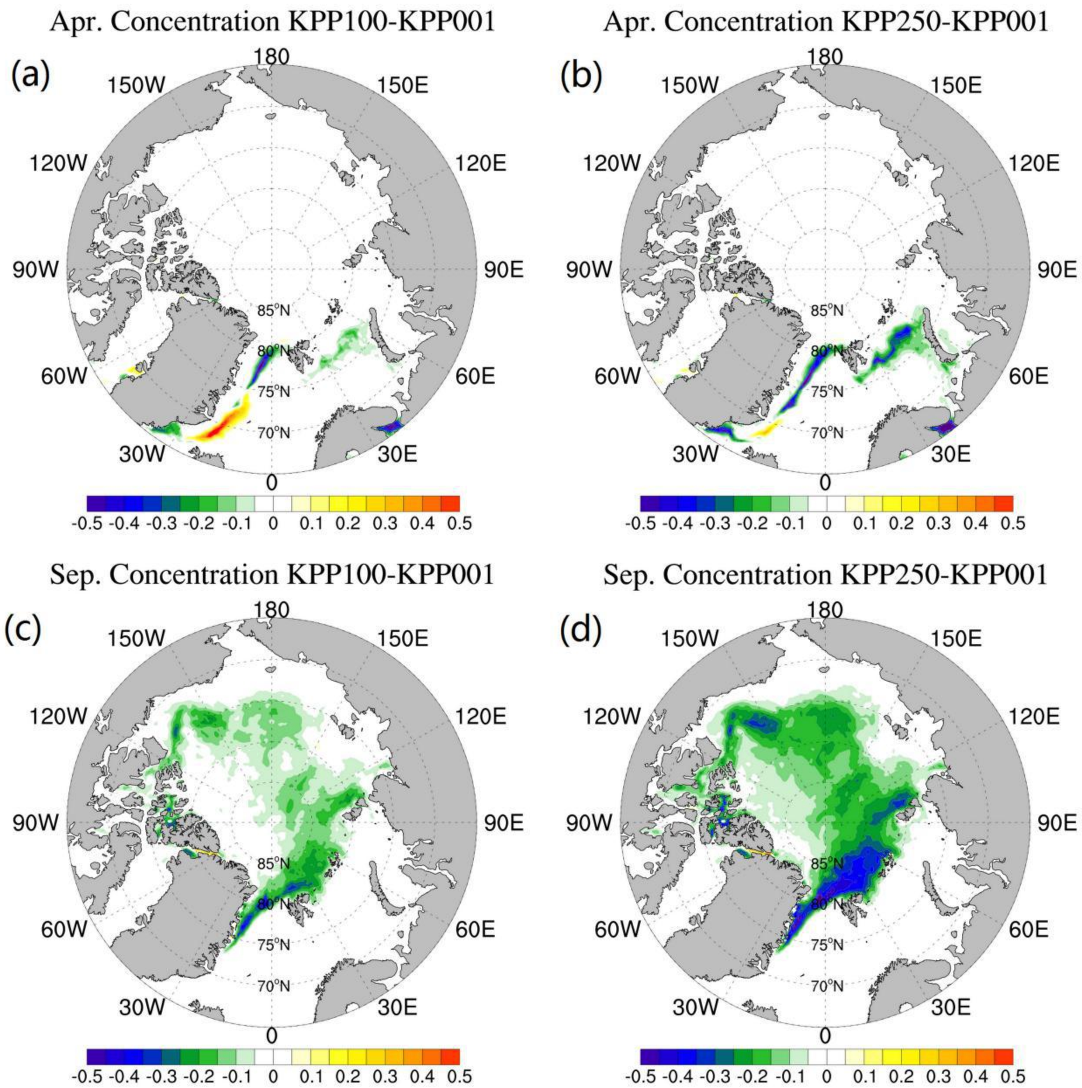

Figure 6. Differences of the 2004-2013 mean sea ice concentration between runs KPP100 and KPP001 (1st column) and between runs KPP250 and KPP001 (2nd column). Rows 1 to 2 show the April sea ice concentration, the September sea ice concentration.

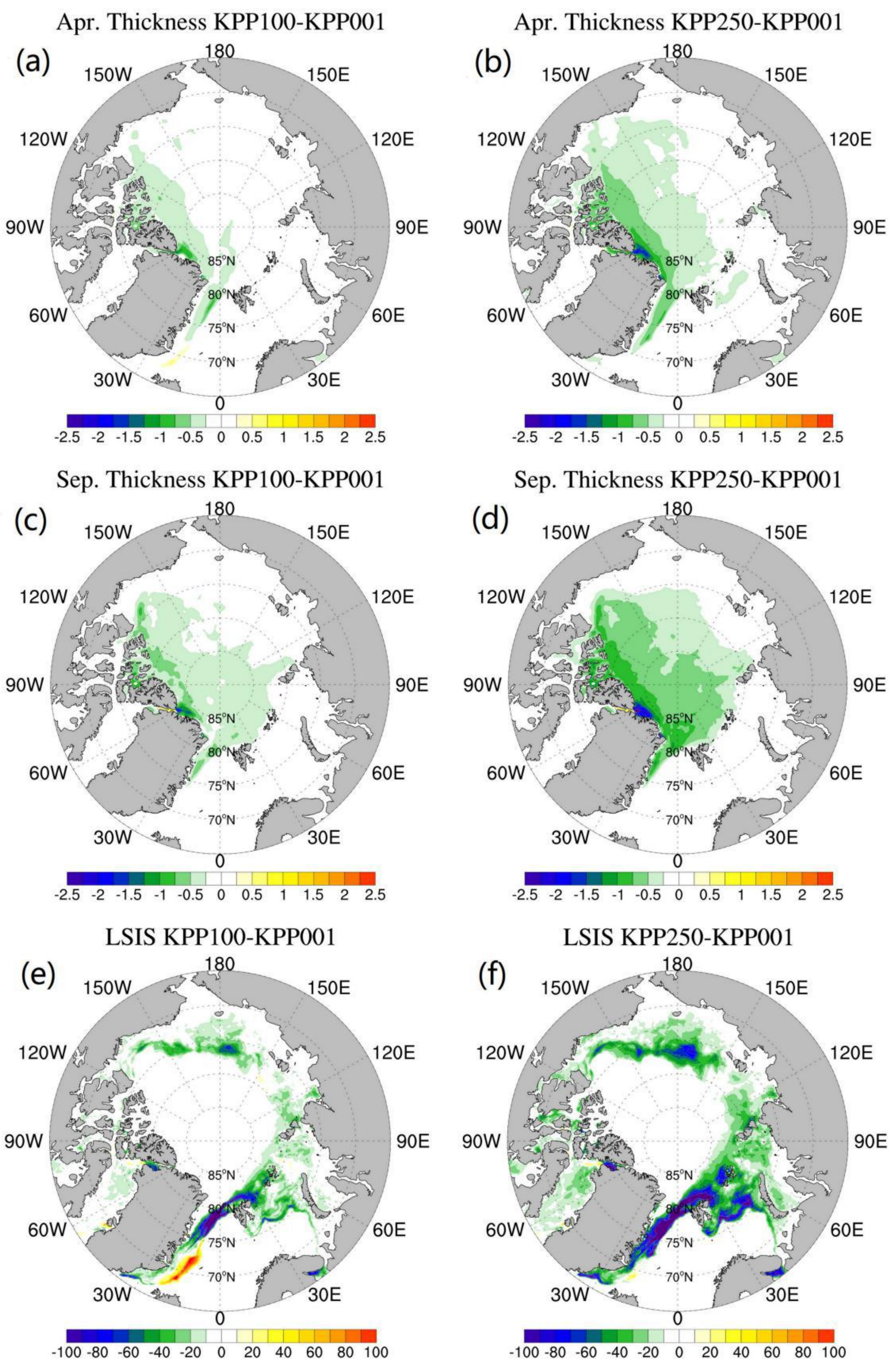

Figure 7. Differences of the 2004-2013 mean sea ice thickness in m and length of sea ice season in days between runs KPP100 and KPP001 (1st column) and between runs KPP250 and KPP001 (2nd column). Rows 1 to 3 show the April sea ice thickness, the September sea ice thickness, the length of sea ice season.

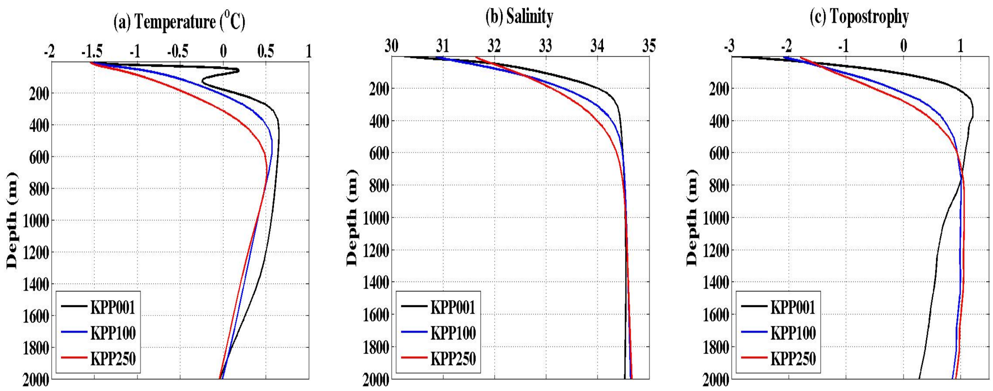

Figure 8. Vertical distributions of spatial averaged (a) ocean temperature in °C, (b) salinity, and normalized spatial integrated (c) topostrophy. Domain used in the calculation cover areas in the Canadian Basin and Eurasian Basin where total depth is larger than 1000 m. The black, blue, red curves represent the KPP001, KPP100, KPP250 runs, respectively.

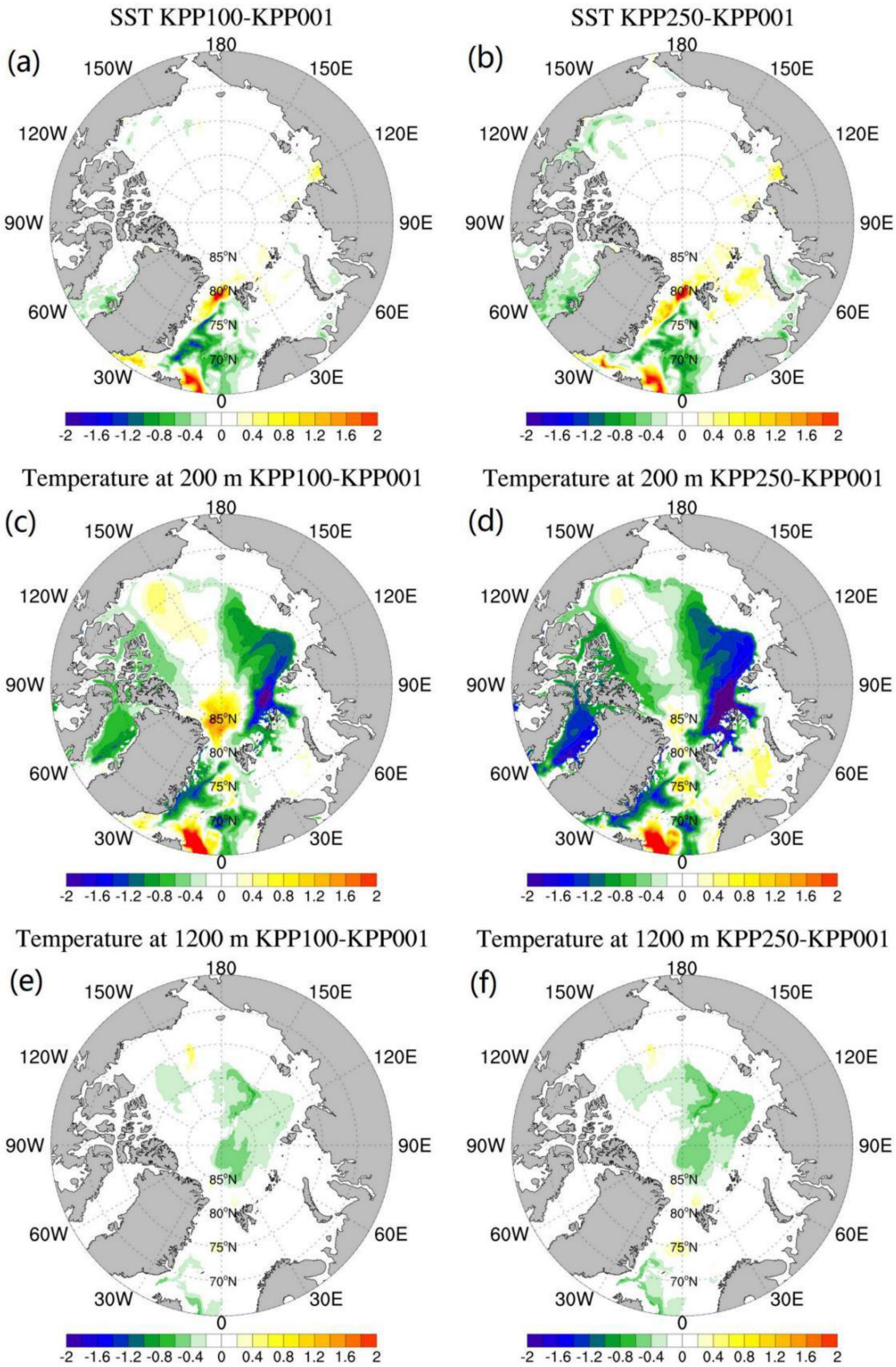

Figure 9. Differences in the 2004-2013 mean ocean temperature in °C at different depths between runs KPP100 and KPP001 (1^{st} column) and runs KPP250 and KPP001 (2^{nd} column). Rows 1 to 3 show surface temperature, temperature at 200 m depth, temperature at 1200 m depth.

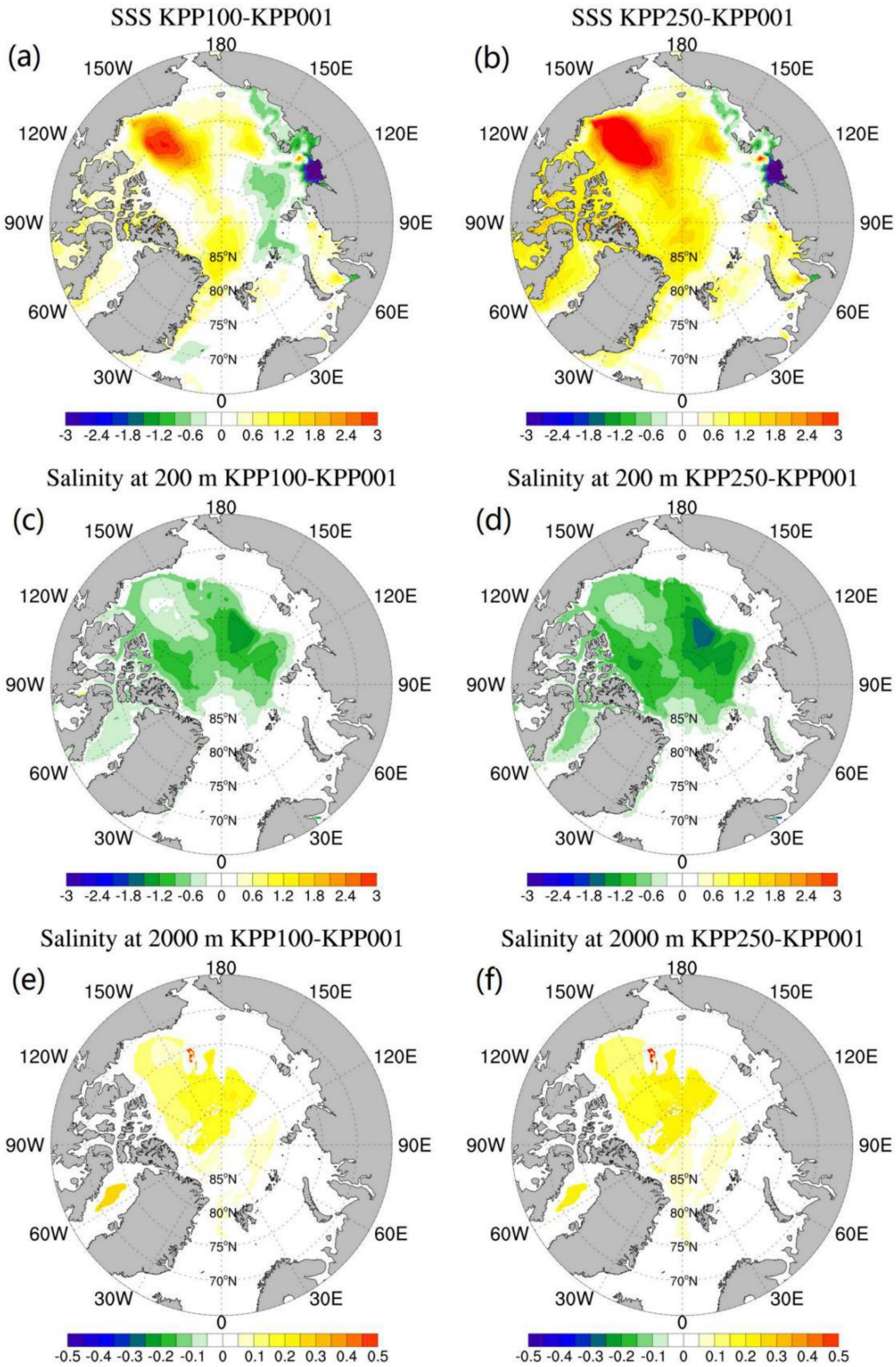

Figure 10. Difference in the 2004-2013 mean ocean salinity between runs KPP100 and KPP001 (1^{nd} column) and runs KPP250 and KPP001 (2^{nd} column) . Rows 1 to 3 show surface salinity, salinity at 200 m depth, salinity at 2000 m depth.

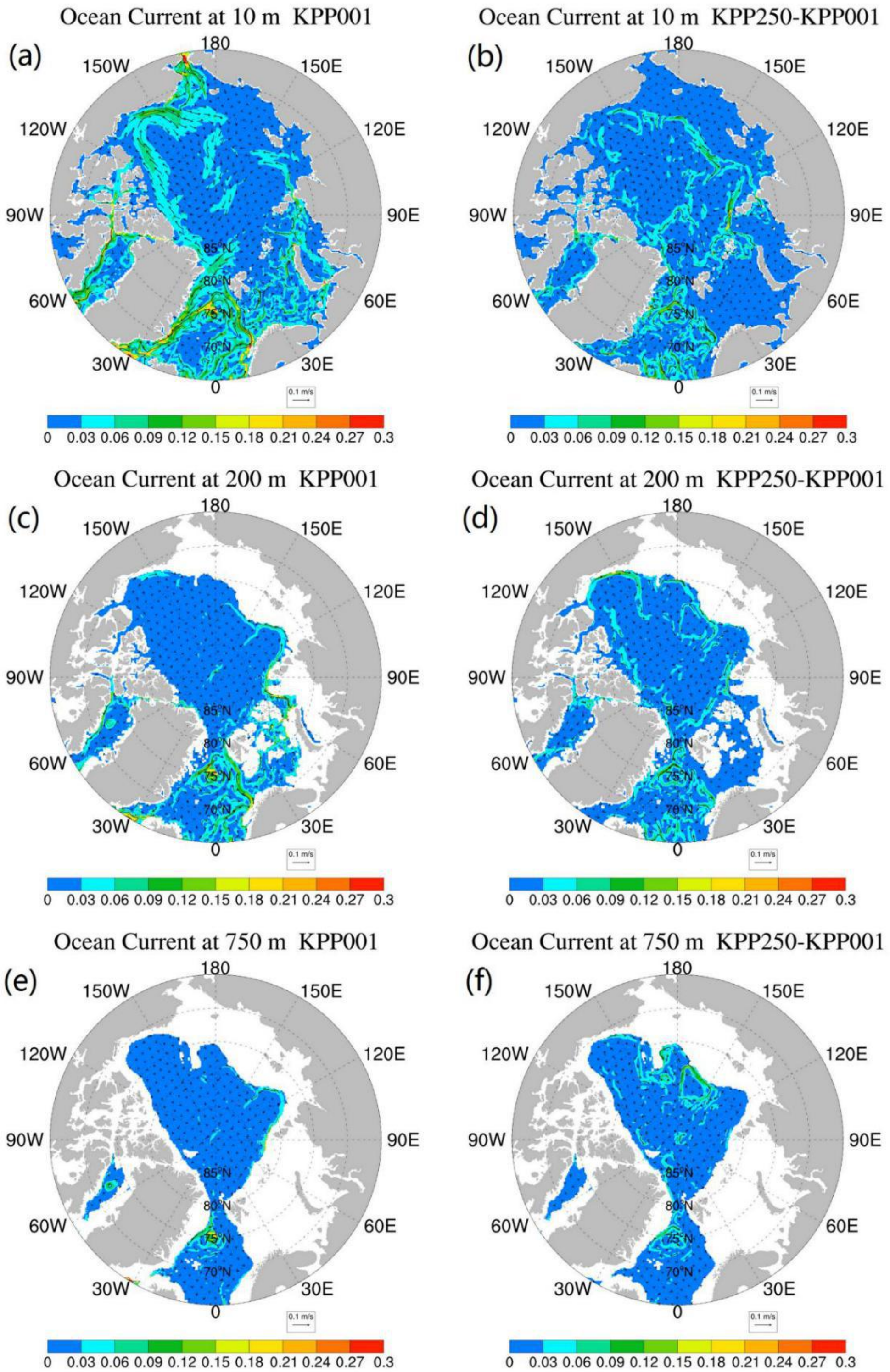

Figure 11. The 2004-2013 mean ocean current in ms^{-1} (1st column) and difference between runs KPP250 and KPP001 (2nd column). Rows 1 to 3 show velocity at 10 m depth, 200 m depth, 750 m depth. Color denotes the absolute velocity.

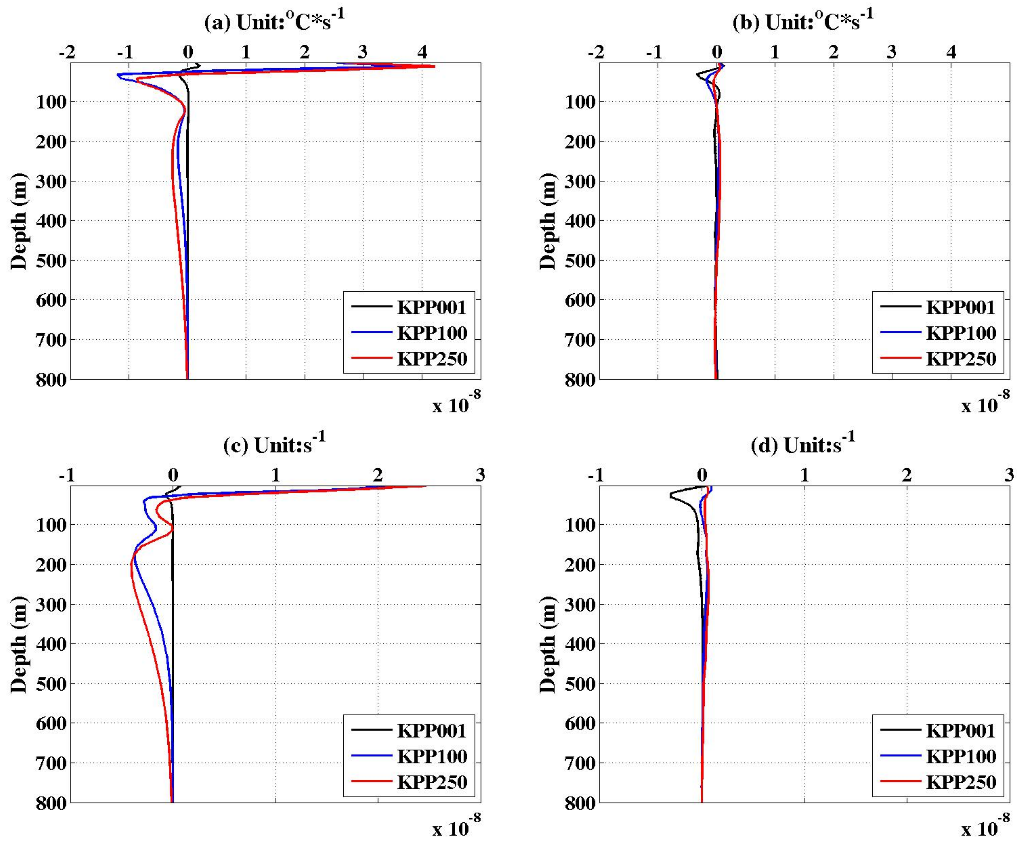

Figure 12. Tracer tendency terms in Canadian Basin and Eurasian Basin. (a) $\frac{\partial T}{\partial t_{bd}}$, (b) $\frac{\partial T}{\partial t_{va}}$, (c) $\frac{\partial S}{\partial t_{bd}}$, (d) $\frac{\partial S}{\partial t_{va}}$. Units for (a) and (b) are °C*s^{-1}. Units for (c) and (d) are s^{-1}. The black, blue, red curves represent the KPP001, KPP100, KPP250 runs, respectively.